Annals of Glaciology

Article

Cite this article: Stewart KD, Palm W, Shakespeare CJ, Kraitzman N (2024). The sensitivity of sea-ice brine fraction to the freezing temperature and orientation. *Annals of Glaciology* **65**, e35, 1–12. https://doi.org/10.1017/aog.2024.36

Received: 4 October 2023
Revised: 29 August 2024
Accepted: 5 September 2024

Keywords:
sea ice; sea-ice growth and decay; sea-ice modelling

Corresponding author:
Kial Douglas Stewart;
Email: kial.stewart@anu.edu.au

The sensitivity of sea-ice brine fraction to the freezing temperature and orientation

Kial Douglas Stewart[1,2], William Palm[1,2], Callum James Shakespeare[1,2] and Noa Kraitzman[3]

[1]Climate & Fluid Physics Laboratory, Australian National University, Acton, Australia; [2]Australian Research Council Centre of Excellence for Climate Extremes, University of New South Wales, Sydney, Australia and [3]School of Mathematical and Physical Sciences, Macquarie University, Sydney, Australia

Abstract

The changing conditions in which sea ice forms and exists are likely to affect the properties of sea ice itself, and potential climate feedbacks need to be identified and understood to improve future projections. Here we perform a set of idealised laboratory experiments that model sea-ice growth under a range of freezing conditions. The results confirm existing theories; sea-ice growth rate is largest for cooler freezing temperatures, fresher ambient salinities and cases with bottom cooling. Our primary metric of interest is the brine fraction (the volume ratio of brine inclusions to the total sea ice), which we quantify and determine its sensitivity with respect to the ambient salinity, freezing temperature and, for the first time, the freezing direction. We find that the brine fraction of our model sea ice is most sensitive to freezing temperature, and increases 2.5% per 1°C increase of freezing temperature.

1. Introduction

Sea ice is a vital component of Earth's climate system, covering more than 10% of the global oceans at least part of each year (Weeks, 2010; Eayrs and others, 2019). The high albedo of the sea ice and overlying snow reflects between 80 and 90% of the incoming solar radiation, thereby strongly limiting the radiative heating of polar surface waters. Brine rejection from sea ice increases the salinity of high-latitude surface ocean waters that ultimately sink and play a key role in the global thermohaline overturning circulation (e.g. Foster and Carmack, 1976; Wakatsuchi and Ono, 1983). Sea ice is also highly sensitive to changes in climate, and is currently exhibiting repeated record low areal coverage (e.g. Purich and Doddridge, 2023), which serves as an important measure of how the Earth system is responding to climate change. For example, the Arctic-Subarctic sea ice has recently shifted from a perennial to a seasonal regime, exhibiting similar levels of seasonality to Antarctic sea ice (Haine and Martin, 2017).

Despite the importance of its role in Earth's climate, and its unique set of dynamics and thermodynamics, the representation of sea ice in coupled climate models is typically fixed to those that best suit the ocean circulation model. That is, a horizontal grid is selected for the ocean processes of interest, and the sea-ice field is discretised onto this ocean-specific grid; the sea-ice state and characteristics are represented with bulk values, and the dynamics/thermodynamics are approximated with a set of continuous partial differential equations that are solved with a timestep selected for the ocean dynamics. Theories and limited existing observations are used to develop parameterisations of small-scale dynamics that relate sub-grid scale processes to the larger scales that are resolved by the horizontal grid. Many dynamics specific to sea ice, in particular its rheology, need to be omitted because they are not well represented by the ocean's horizontal grid. Nevertheless, sea-ice model development continues to improve and include additional processes, whose representation in turn often require new parameterisations. For example, the latest version of the CICE sea-ice model (CICE6 v6.1.2) includes a capability for a floe size distribution, which then permits lateral sea-ice growth/melt dynamics, which requires specific parameterisations that are distinct from vertical sea-ice growth/melt. This new feature raises the question of whether the direction of sea-ice growth changes the bulk characteristics of the sea-ice itself (e.g. Scotti and others, 2019).

The difficulties associated with the realistic representation of sea ice in climate models are a major scientific challenge for predicting future climate states. Sea ice is a particularly sensitive entity in the climate system and prone to feedback cycles, as demonstrated by the ice-albedo phenomenon (e.g. Budyko, 1969). The polar amplification of global warming (e.g. Manabe and Stouffer, 1979) will tend to warm the surface atmosphere at higher latitudes faster than lower latitudes; this will result in sea ice growing in conditions that are relatively warmer than before (e.g. Post and others, 2019). Understanding how sea-ice properties respond to warmer freezing temperatures is an important step for improving sea ice and climate models.

Here, we investigate the impacts of freezing temperature and direction on the brine fraction of sea ice by conducting a suite of laboratory experiments to model sea-ice growth across a range of freezing temperatures and directions. The bulk brine fraction of the model sea ice was estimated using two independent approaches, and found to be sensitive to both the freezing temperature and direction across a wide range of ambient salinities. In section 2 we provide

cambridge.org/aog

background context for our study and subsequent analysis. In section 3 we describe the laboratory apparatus, methodology and analysis, and we present and discuss the results of the experiments in section 4. We provide a brief commentary on the geophysical implications of our results in section 5.

2. Background

Sea ice exists in some of the least hospitable regions on Earth, imposing significant challenges for obtaining direct observations of small-scale properties. Indeed, much of our existing knowledge of sea-ice thermodynamics is based on controllable laboratory experiment (e.g. Cox and Weeks, 1975; Wettlaufer and others, 1997). Seawater is a multi-component liquid wherein its constituents have different freezing points. In such a system, the freezing process typically results in the formation of a porous mixture of solid ice, liquid inclusions and trapped air bubbles, collectively known as a mushy layer (e.g. Worster, 1997; Feltham and others, 2006; Wells and others, 2019). Solidification at temperatures above the melting temperature of the constituents results in the solvent freezing whilst the solutes remain liquid. In the case of an aqueous solution containing salts, like seawater, as solidification occurs, finger-like solid crystals known as dendrites grow in advance of the solidifying face. These dendrites cannot incorporate the dissolved salts into their crystalline structure and expel them into the solution between the solid crystals (Anderson and Guba, 2020). This enriched saline solution is referred to as brine. As the dendrites continue to grow and the ice face advances, some of the liquid brine becomes trapped within the solid ice matrix, forming brine inclusions. These liquid brine inclusions, aided by gravity, are able to migrate through the solid ice, merging and forming brine channels in the ice matrix. The brine eventually drains into the ocean below via a convective overturning process in which relatively fresher ocean water replaces the brine in the channels. The mixture of solid ice, brine inclusions and air bubbles forms the mushy layer (Feltham and others, 2006). This mixture is generally classified by its solid fraction, which is the ratio of the solid ice volume to the total volume of the mushy layer; the solid fraction is related to the brine fraction (the ratio of the liquid brine volume to the total mushy layer volume, which is often employed in sea-ice models) and, for negligible volumes of trapped air bubbles, they sum to unity.

Mushy layers are prevalent on Earth and form from both natural and industrial processes, such as the solidification of Earth's core, magma and metallic alloys (Huppert, 1990; Peppin and others, 2007; Anderson and Guba, 2020). In the case of seawater, during the formation of sea ice, salts from the seawater are rejected from the ice lattice to form highly saline brine inclusions. The high salinity of these brine inclusions results in them remaining in liquid phase within the ice; that is, in temperature–salinity space they exist to the right of the liquidus curve (e.g. Fig. 1).

Mushy layers are subject to chemical and thermodynamic processes, and as such they react and evolve as the mushy layer grows (Wells and others, 2019; Anderson and Guba, 2020). For example, brine inclusions must be in thermodynamic equilibrium within the ice. If they are not, heat will flow to negate the temperature gradient such that thermodynamic equilibrium is established. Therefore, due to the low temperatures within mushy layers, in order for the brine inclusions to remain liquid, they must exist on their liquidus curve, the solid–liquid phase transition point of a given substance. This requires brine inclusions to vary their chemical and temperature characteristics as the mushy layer varies in temperature, which results in a reactive medium.

Huppert (1990) demonstrated that solidification of solutions with multiple dissolved salts below the eutectic temperature (the minimum temperature where all salts are able to be in solution) creates a compositional mushy layer; that is, an ice matrix which contains crystals of solid salt. Here we avoid the added complexity of compositional mushy layers and focus on solidification at temperatures above the eutectic temperature for our aqueous solution. We model the seawater and sea ice with a single-component liquid that is sodium chloride (NaCl) and fresh tapwater, which has a single eutectic temperature of $T_e = -21.1$°C. Note that actual seawater and sea ice, as a material composed of several different salts, does not have a single eutectic point, and there is still liquid brine for temperatures below −70°C, however precipitation begins at $T_e < -21.1$°C (e.g. Weeks and Ackley, 1986), and modern sea-ice models employ an equation of state with an imposed eutectic temperature of −36.2°C (e.g. Vancoppenolle and others, 2019).

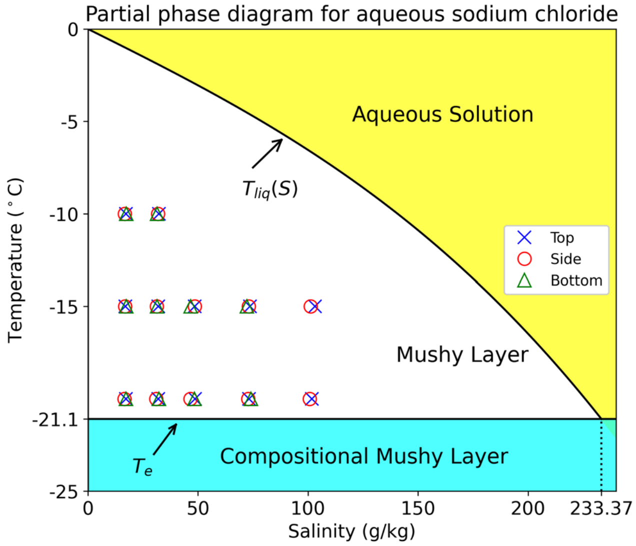

Figure 1. A partial phase diagram for aqueous sodium chloride solutions. The blue region is cooler than the eutectic temperature $T_e = -21.1$°C for aqueous sodium chloride solutions, at which point the sodium chloride crystal precipitate out of solution. The white region represents the mushy layer regime, and the yellow region represents the regime of aqueous solution wherein the salinity is too large for ice to form for the given temperature; these regimes are separated by the liquidus curve, which is given by T_{liq} (Eqn (8)) for temperatures warmer than eutectic temperature. The crosses, circles and triangles represent the initial ambient salinities and freezing plate temperatures of the experiments with top, side and bottom freezing directions, respectively.

The temperature difference between the relatively warmer ocean and relatively cooler atmosphere means that vertical temperature gradients exist within sea ice. It follows that a similar temperature gradient exists within and surrounding individual brine inclusions (e.g. Kraitzman and others, 2022). For a brine inclusion to maintain phase equilibrium, a salinity gradient is necessary within the liquid brine inclusions, which requires saltier, cooler liquid to exist at the top of the inclusion (Notz and Worster, 2009). Obviously this arrangement is gravitationally unstable, and the brine inclusion itself is likely to be well-mixed. That is, while the bulk-average of the brine inclusion is likely to be in thermal and chemical equilibrium, the upper and lower regions of the brine inclusion are not able to achieve equilibrium with their respective surrounds and will exist on either side the liquidus curve; the brine in the upper regions of the inclusion will tend to freeze, while sea ice surrounding the lower regions will tend to melt (e.g. Weeks, 2010). This process is known as Temperature Gradient Zone Melting (TGZM; e.g. Pfann, 1955); in the context of sea ice it is referred to as brine diffusion (e.g. Notz and Worster, 2009), and allows the brine inclusions to migrate through the sea ice which results in the brine inclusions travelling from the upper, cooler to the lower, warmer regions of the sea ice, and ultimately into the ocean below. In the absence of a source of salt in the upper sea-ice region (e.g. neglecting, for instance, sea spray or surface waves depositing salt on the sea-ice upper surface), the migration of brine results in a monotonic decrease in the bulk sea-ice salinity in time. Additionally, and directly relevant to our experiments herein, the direction of the temperature gradient within the sea ice determines the migration direction of brine inclusions; that is, horizontal temperature gradients should result in horizontal migration.

While the process of brine diffusion provides an intuitive example of how brine inclusions are able to remain mobile within a solid ice matrix, its overall effect on the desalination of sea ice is known to be negligible (e.g. Untersteiner, 1968; Notz and Worster, 2009). Gravity drainage is a substantially more effective process for the desalination of sea ice. The morphology of sea ice, and particularly the mushy layer, is such that brine inclusions can develop as channels or chimneys, which often provide a direct link between the internals of the ice and the surrounding solution (e.g. Worster, 1997). In the case of sea ice, the highly saline and near-freezing brine inclusions are much denser than the ocean waters immediately below. Therefore, brine inclusions are negatively buoyant and brine channels can facilitate convective fluid processes between sea ice and sea water (Worster and Rees Jones, 2015). Convective motion expels saline brine into the underlying ocean, in a process known as gravity drainage. As brine channels provide a direct and active mechanism to drive flow between sea ice and the ocean, gravity drainage governs the rate of brine rejection. Due to continuity, the volume of brine expelled from ice must be replaced, resulting in relatively less saline seawater replacing brine in the mushy layer (Wettlaufer and others, 1997). As thermodynamic and chemical equilibrium must again be established, the less saline seawater in the ice freezes, re-initiating solidification and hence, increasing the solid fraction, and altering the mushy layer structure. Given that gravity drainage fluxes brine downwards, the freezing direction of sea ice may influence how effective gravity drainage is in facilitating brine rejection.

3. Laboratory experiments

3.1 Apparatus

Our experiments investigating ice growth were conducted in the Climate and Fluid Physics (CFP) laboratory at the Australian National University. The experimental apparatus consisted of a well-insulated, sealed, fluid-filled tank with internal dimensions $30.5 \times 21.5 \times 17.5\ \text{cm}^3$ (see Fig. 2), of a similar design to that used by Wettlaufer and others (1997). The two smallest area sidewalls of the tank were copper plates in direct thermal contact with controllable heat exchangers that allowed the sidewall temperatures to be independently prescribed; the other four sidewalls were double-glazed perspex. The tank was positioned between an illuminated white LED screen and a Basler AG camera that viewed the entire tank volume and configured such that it was able to clearly distinguish between the ambient fluid and the growing ice. The apparatus was in a section of the CFP laboratory that was climate controlled and maintained at a constant temperature of 22.5 ± 0.2°C.

Two independent Julabo FP50 HL refrigerating/heating constant temperature baths were used to prescribe the copper sidewall temperatures. These constant temperature Julabo units pumped ethanol through the sidewall heat exchangers, thereby providing an operational sidewall temperature range that easily spanned from below the eutectic temperature of salty water ($T_e = -21.1$°C) to above the freezing point of fresh water. During operation, one of these copper sidewall plates was set to a temperature below the freezing point of the fluid, with the other plate used to maintain the temperature of the ambient fluid; these were referred to as the ‘freezing’ and ‘ambient’ plates, respectively. So while the freezing plate initiates ice growth, the primary purpose of the ambient plate was to negate any unwanted heat flux into the tank from the laboratory, thereby maintaining the temperature of the ambient close to its freezing temperature. The ambient fluid was kept well-mixed and homogeneous by way of an external pump that withdrew ambient fluid from the ‘upper’ region of the tank (‘upper’ in the sense of the side cooling cases) and gently re-injected it through a shrouded perforated tube in the vicinity of the ambient plate, thereby inhibiting the formation of stratification. The temperature of the ambient was logged using a thermistor positioned in the centre of the tank.

The effect of the freezing direction was one of the variables of interest. For this, the tank was mounted in a semicircular frame that was able to be tilted such that the freezing plate could be oriented at the top, side or bottom of the tank.

As ice grew against the freezing plate, there was an increase in total volume that was associated with the phase change from liquid to ice. This volume increase was accommodated by a displacement of ambient fluid through an expansion tube and into

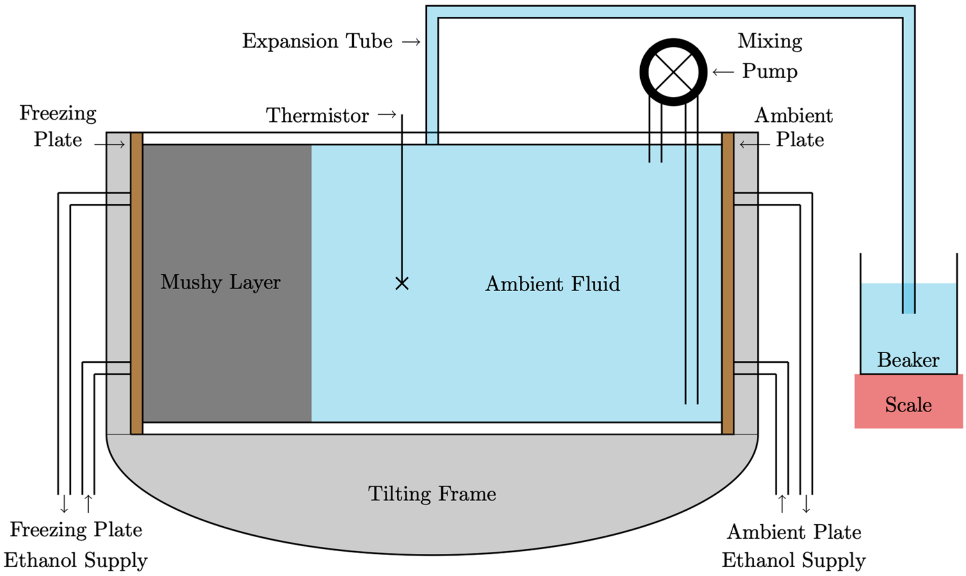

Figure 2. A two-dimensional schematic of the experiment apparatus.

a beaker that was on a scale, which recorded the measured mass in time.

3.2 Methodology

The tank was tilted in the desired orientation and the tank, expansion tube and scale beaker were carefully filled with a de-aired solution of water with a precisely known salinity. The open end of the expansion tube was placed within the scale beaker below the water level, thereby creating a closed system that was able to accommodate any volume changes in the tank. The mixing pump was switched on to keep the ambient fluid well-mixed. Both of the constant temperature sidewalls were set to ∼2°C above the estimated freezing temperature for the particular ambient salinity, and the system was left to come to thermal equilibrium, which typically involved a slight contraction of volume in the tank and an associated drawing of fluid from the scale beaker. Over time, the mass measured by the scale adjusted to become steady, at which time the experiment was ready to begin.

The freezing plate temperature was lowered to a desired point below the ambient freezing temperature, initiating ice growth on the plate. The ambient plate temperature was maintained just above the ambient freezing temperature. These thermal boundary conditions were maintained for a period of over 24 h, during which time the ambient temperature and beaker mass were logged, and high-resolution images from the Basler AG camera recorded at 30 min intervals. After this ∼24 h logging period, the freezing plate temperature was returned to that of the ambient plate and the ice was allowed to melt back into the mixed ambient fluid. Once the ambient fluid returned to thermal equilibrium, the next experiment was commenced with a different prescribed freezing plate temperature and/or tank orientation. The ambient fluid was completely replaced between experiments with different initial ambient salinities.

3.3 Parameter space

The freezing plate temperatures T_{FP} explored here were −10C, −15C and −20°C, which were all warmer than the eutectic temperature of salty water at which compositional mushy layers form ($T_{\mathrm{e}} = -21.1$°C). The initial ambient salinities employed here were approximately 17, 33, 48, 73 and 102 g kg^{-1}; these were selected to be within the range explored by Wettlaufer and others (1997) to allow for direct comparison between our studies. For initial salinities greater than 45 g kg^{-1}, the warmest freezing temperature setting ($T_{\mathrm{FP}} = -10$°C) did not produce sufficiently detectable ice, so only freezing temperatures of $T_{\mathrm{FP}} = -15$°C and $T_{\mathrm{FP}} = -20$°C were used. For the highest salinity experiments (102 g kg^{-1}), ice produced in the case of bottom cooling was too buoyant and would detach from the freezing plate and float up through the ambient and melt, so only the top and side cooling cases are included here. This approach provides a set of 34 different experiments, for which the initial ambient salinities, freezing temperature settings and tank orientations are depicted in Figure 1.

3.4 Analysis: calculating the bulk solid fraction

The quantitative diagnostics here are the logs of the ambient fluid temperature and beaker mass, and the high-resolution images, which combine to provide estimates of the bulk solid fraction ϕ of the mushy layer. The solid fraction is defined by the ratio of the volume of solid ice to the total volume of the mushy layer,

$$\phi = \frac{V_{\mathrm{s}}}{V_{\mathrm{b}} + V_{\mathrm{s}}}, \tag{1}$$

where V_{s} and V_{b} refer to volumes of solid ice and liquid brine (m^3), respectively. A solid fraction of $\phi = 1$ represents solid ice with no liquid brine, and a value of $\phi = 0$ is entirely liquid brine without any solid ice. Note that for negligible volumes of trapped air bubbles, the solid fraction ϕ and the brine fraction ϕ_{l} ($\phi_{\mathrm{l}} = V_{\mathrm{b}}/(V_{\mathrm{b}} + V_{\mathrm{s}})$), which is often used in sea-ice models in place of the solid fraction (e.g. Hunke and others, 2015), sum to unity; $\phi + \phi_{\mathrm{l}} = 1$. The definition above describes a bulk solid fraction which is useful as it provides a domain average of the varying fine scale structures, such that the large-scale properties of the mushy layer can be characterised. Here, we follow Wettlaufer and others (1997) by employing two distinct approaches to estimate the bulk solid fraction in our experiments; these are based on the conservation of salt and the conservation of mass, respectively, and are described below. Note that in reality the solid fraction exhibits variability within the sea ice, which is not able to be captured with our bulk conservation methods employed here.

3.4.1 Bulk salt mass conservation method

The total conservation of mass of salt requires the total mass of salt in the system to remain constant throughout the experiment, that is,

$$\underbrace{S_{\mathrm{o}}\rho_{\mathrm{o}}V_{\mathrm{t}}}_{\text{Initial salt}} = \underbrace{(1-\phi)S_{\mathrm{b}}\rho_{\mathrm{b}}V_{\mathrm{m}}}_{\text{Brine inclusions}} + \underbrace{S_{\mathrm{a}}\rho_{\mathrm{a}}(V_{\mathrm{t}} - V_{\mathrm{m}})}_{\text{Ambient fluid}} + \underbrace{S_{\mathrm{e}}m_{\mathrm{e}}}_{\text{Expelled fluid}}, \tag{2}$$

where S_{o}, S_{b}, S_{a} and S_{e} refer to the salinities of the initial ambient fluid, brine inclusions, ambient fluid during ice growth and expelled fluid in the beaker, respectively (g kg^{-1}); ρ_{o}, ρ_{b} and ρ_{a} are the densities of the initial ambient fluid, brine inclusions and ambient fluid during ice growth, respectively (kg m^{-3}); V_{t} and V_{m} refer to the volumes of the tank and mushy layer, respectively (m^3); and m_{e} is the mass of ambient fluid expelled into the beaker (kg).

Rearranging Eqn (2) for the solid fraction produces,

$$\phi_S = \frac{S_{\mathrm{o}}\rho_{\mathrm{o}}V_{\mathrm{t}} - S_{\mathrm{b}}\rho_{\mathrm{b}}V_{\mathrm{m}} - S_{\mathrm{a}}\rho_{\mathrm{a}}(V_{\mathrm{t}} - V_{\mathrm{m}}) - S_{\mathrm{e}}m_{\mathrm{e}}}{-S_{\mathrm{b}}\rho_{\mathrm{b}}V_{\mathrm{m}}}, \tag{3}$$

where we use the subscript S identify this solid fraction estimate as that provided by the mass of salt conservation method.

3.4.2 Bulk total mass conservation method

The conservation of total mass provides a mass-balance model for the solid fraction ϕ where the mass of the expelled fluid is directly measured, and the masses of the initial system, solid ice, brine inclusions, evolving ambient fluid are estimated by the products of their respective densities and volumes. That is,

$$\underbrace{\rho_{\mathrm{o}}V_{\mathrm{t}}}_{\text{Initial mass}} = \underbrace{\phi\rho_{\mathrm{ice}}V_{\mathrm{m}}}_{\text{Solid ice}} + \underbrace{(1-\phi)\rho_{\mathrm{b}}V_{\mathrm{m}}}_{\text{Brine inclusions}} + \underbrace{\rho_{\mathrm{a}}(V_{\mathrm{t}} - V_{\mathrm{m}})}_{\text{Ambient fluid}} + \underbrace{m_{\mathrm{e}}}_{\text{Expelled fluid}}, \tag{4}$$

where ρ_{o}, ρ_{ice}, ρ_{a} and ρ_{b} are the densities of the initial ambient fluid, solid ice, ambient fluid during ice growth and brine channel fluid, respectively (kg m^{-3}); V_t and V_m refer to the volumes of the tank and mushy layer, respectively (m^{-3}); and m_e is the mass of ambient fluid expelled into the beaker (kg). Equation (4) can then be rearranged for ϕ, to provide the total mass conservation method for estimating the solid fraction of mushy layer, that is,

$$\phi_M = \frac{\rho_o V_t - m_e - \rho_a (V_t - V_m) - \rho_b V_m}{(\rho_{ice} - \rho_b) V_m}, \qquad (5)$$

where we use the subscript M to identify this solid fraction estimate as that provided by the total mass conservation method.

3.4.3 Quantifying terms for the conservation methods

The mass of the fluid expelled into the beaker, m_e, was logged in time for the duration of each experiment. The salinity of the expelled fluid S_e was calculated from direct measurements of its density ρ_e with a precision Anton–Paar densimeter and the equation of state for NaCl and fresh tapwater given by Notz (2005),

$$\rho_e = 998.43 + 0.69722 S_e + 2.5201 \times 10^{-4} S_e^2, \qquad (6)$$

which was intended for salinities up to $S = 260$ g kg^{-1} and temperatures between 0 and –20°C from the data of Weast (1971); note that for this temperature range, the maximum error from neglecting the temperature dependence of the density is 2% (Notz, 2005).

The volume of the tank V_t was constant and determined from accurate measurements of the tank geometry. The initial ambient fluid density ρ_o was directly measured with a precision Anton-Paar densimeter. The initial ambient fluid salinity S_o was calculated from its density with Eqn (6).

Following Notz (2005), we estimate the density of the solid ice ρ_{ice} with the equation of state given by Pounder (1965),

$$\rho_{ice} = 916.8 - 0.1403 T_{ice}, \qquad (7)$$

where T_{ice} was the solid ice temperature in °C. As we do not have direct measurements of temperature within the solid ice, we approximated it as the mid-point between the freezing plate temperature T_{FP} and the ambient fluid–ice interface temperature T_{liq}. The interface temperature T_{liq} was assumed to be the liquidus temperature for water with the ambient salinity S, given by Weast (1971) as,

$$T_{liq}(S) = -5.92 \times 10^{-2} S - 9.37 \times 10^{-6} S^2 - 5.33 \times 10^{-7} S^3, \qquad (8)$$

for the range of S up to 230 g kg^{-1}. Thus,

$$T_{ice}(S) = \frac{T_{FP} + T_{liq}(S)}{2}, \qquad (9)$$

which is used in Eqn (7) to give us the density of solid ice ρ_{ice}.

The thickness of the mushy layer h increased as the ice grows; this thickness was estimated from the high-resolution images captured throughout the experiments. The light intensity discontinuity across the mushy layer and liquid ambient boundary was identified with image analysis software and used to calculate the tank-average thickness of the mushy layer. This mushy layer thickness was multiplied by the relevant geometry of the tank to obtain an estimate of the mushy layer volume V_m. This simple approach assumes there was no three-dimensional structure in the mushy layer growth, which in reality was not the case. To account for three-dimensionality in the mushy layer, a small geometrical volume correction was applied (described below). Note that the initial mushy layer thickness h_o was not necessarily zero; the first photo of the experiment was typically 30 min after the freezing plate temperature has been adjusted. The final mushy layer thickness h_f was the thickness of the mushy layer when it had reached an equilibrium, which was defined as the time when the average mushy layer thickness had not increased by more than 0.5% relative to the previous image.

The salinity of the brine inclusions S_b was assumed to be the salinity corresponding to the boundary between mushy layer and aqueous solution for that particular ice temperature, which was given by the liquidus curve. That is, the equation for the liquidus (Eqn (8)) can be inverted to give brine salinity as a function of ice temperature (°C),

$$S_b = -17.6 T_{ice} - 0.389 T_{ice}^2 - 3.62 \times 10^{-3} T_{ice}^3. \qquad (10)$$

With the brine salinity we then estimated the brine density with Eqn (6). Note that this equation for brine salinity as a function of ice interior temperature is specific for aqueous solutions of NaCl and water, and differs from that employed by sea-ice models (Hunke and others, 2015),

$$S_b = \left(10^{-3} - \frac{0.054}{T_{ice}}\right)^{-1}, \qquad (11)$$

which is specific for brine salinity in sea ice formed from actual seawater.

The final salinity of the ambient fluid S_f was calculated from the final density of the ambient fluid ρ_f, which was measured directly with a precision Anton-Paar densimeter, and Eqn (6). The evolving ambient fluid density ρ_a, however, was not measured during the experiment, so the evolving salinity of the ambient fluid S_a needed to be estimated using measurements of the initial and final ambient fluid salinities, S_o and S_f, respectively. The salinity of the ambient fluid evolved due to the growth of the mushy layer and the brine rejection from the mushy layer; these processes were not constant in time, so approximating the ambient fluid salinity with a linear evolution between the initial and final salinities was not valid. Indeed, in several (but not all) of the experiments we directly measured the ambient salinity evolution (by way of a conductivity probe in the beaker) and found it to have an initial period of relatively rapid adjustment before asymptoting towards the final ambient salinity. Thus, we followed the approach of Wettlaufer and others (1997), and related the evolution of the ambient salinity to the evolution of the mushy layer thickness h by way of a non-dimensional scaling factor; that is,

$$H_c = \frac{h(t) - h_o}{h_f - h_o}, \qquad (12)$$

where $h(t)$ was the mushy layer thickness at time t, and h_o and h_f were the initial and final mushy layer thicknesses. Note that this non-dimensional scaling factor H_c goes from 0 to 1 as time increases, and has the same (non-linear) shape of temporal evolution as $h(t)$. The estimated salinity of the ambient fluid was then approximated as,

$$S_a(t) = H_c (S_f - S_o) + S_o. \qquad (13)$$

The directly measured ambient salinities exhibited good agreement with this ambient salinity approximation. The temperature of the ambient fluid T_a was directly measured and logged throughout the experiment. The evolving density of the ambient fluid ρ_a was then able to be calculated from the ambient fluid temperature and salinity with an appropriate equation of state, for which we used Eqn (6).

In summary, the total mass and salt mass conversation methods require the knowledge of several salinities, temperatures, densities, masses, volumes and thicknesses. Some were directly measured (V_t, m_e, ρ_e, ρ_o, ρ_f, T_a), some were estimated from high-resolution photos (h, h_o, h_f, V_m), and some were approximated from established and/or adapted relationships (S_e, S_o, ρ_{ice}, T_{ice}, T_{liq}, S_b, ρ_b, S_f, S_a, ρ_a). Table 1 lists the terms and their descriptions used for the experiments and subsequent analysis.

Table 1. Terms needed for the conservation methods

Term	Units	Description	Provenance
h	m	Mushy layer thickness	Estimated from photos
h_o	m	Initial mushy layer thickness	Estimated from photos
h_f	m	Final mushy layer thickness	Estimated from photos
V_t	$\mathrm{m^3}$	Volume of tank	Directly measured
V_m	$\mathrm{m^3}$	Volume of mushy layer	Needs h
m_e	kg	Mass of expelled fluid	Directly measured and logged
ρ_e	$\mathrm{kg\ m^{-3}}$	Density of expelled fluid	Directly measured
S_e	$\mathrm{g\ kg^{-1}}$	Salinity of expelled fluid	Eqn (6); needs ρ_e
ρ_o	$\mathrm{kg\ m^{-3}}$	Initial ambient fluid density	Directly measured
S_o	$\mathrm{g\ kg^{-1}}$	Initial ambient fluid salinity	Eqn (6); needs ρ_o
ρ_{ice}	$\mathrm{kg\ m^{-3}}$	Density of solid ice	Eqn (7); needs T_{ice}
T_{ice}	°C	Interior temperature of solid ice	Eqn (9); needs T_{liq}
T_{liq}	°C	Liquidus temperature	Eqn (8); needs S_a
S_b	$\mathrm{g\ kg^{-1}}$	Salinity of brine inclusions	Eqn (10); needs T_{ice}
ρ_b	$\mathrm{kg\ m^{-3}}$	Density of brine inclusions	Eqn 6
ρ_f	$\mathrm{kg\ m^{-3}}$	Final ambient fluid density	Directly measured
S_f	$\mathrm{g\ kg^{-1}}$	Final ambient fluid salinity	Eqn (6); needs ρ_f
S_a	$\mathrm{g\ kg^{-1}}$	Salinity of the ambient fluid	Eqn (13); needs S_o, S_f, h, h_o, h_f
T_a	°C	Temperature of the ambient fluid	Directly measured and logged
ρ_a	$\mathrm{kg\ m^{-3}}$	Density of the ambient fluid	Eqn (6); needs S_a

4. Results

Once the experiments began, the mushy layer was observed to form on the freezing plate within the first 30 mins. The initial distribution of the mushy layer was uniform across the freezing plate, indicative of a uniform boundary condition imposed by the heat exchanger. In time, the edges of the mushy layer within ~5 mm of the tank sidewalls and ice face became rounded, suggesting a small amount of unintentional heat entering the tank from the laboratory; for the bottom cooling case, this rounded mushy layer edge was more obvious (Fig. 3). Also, when estimating the mushy layer volume from the high-resolution photos, a minor geometric correction is applied to account for the mushy layer having rounded edges. As the mushy layer continued to grow, the ice face tended to develop small-amplitude, large-scale three-dimensional structures in the plane parallel to the freezing plate (vertical and into the page in Fig. 2; visible in the top cooling case photo in Fig. 3). The exact nature of these structures appeared to depend on minor differences in initial conditions since repeating experiments didn't necessarily reproduce identical shapes of mushy layer face structures. Experiments with bottom cooling exhibited relatively less three-dimensionality to the mushy layer face, suggesting the structure was perhaps related to the gravity drainage process in the top and side cooling cases. Nevertheless, the amplitude of these features was small relative to the mushy layer thickness; as such, the mushy layer thickness and volume estimates were developed by taking a tank average of all ice edges visible. The detection limit of this method was given by the thickness per pixel, which is approximately 0.7 mm per pixel. Considering the complications associated with the rounded edges and three-dimensionality corrections, generous uncertainties (up to 5%, depending on the extent of the rounded edges and three-dimensionality) were applied to the mushy layer volume estimates.

Analysis of the high-resolution photos allowed us to quantify the bulk mushy layer thickness and how it changed over the course of an experiment (Fig. 4). For all experiments, the mushy layer thickness monotonically increased in time, with the rate of thickness change tending to decrease in time. The responses of the mushy layer thickness to the initial ambient salinity and freezing plate temperatures were intuitive and consistent

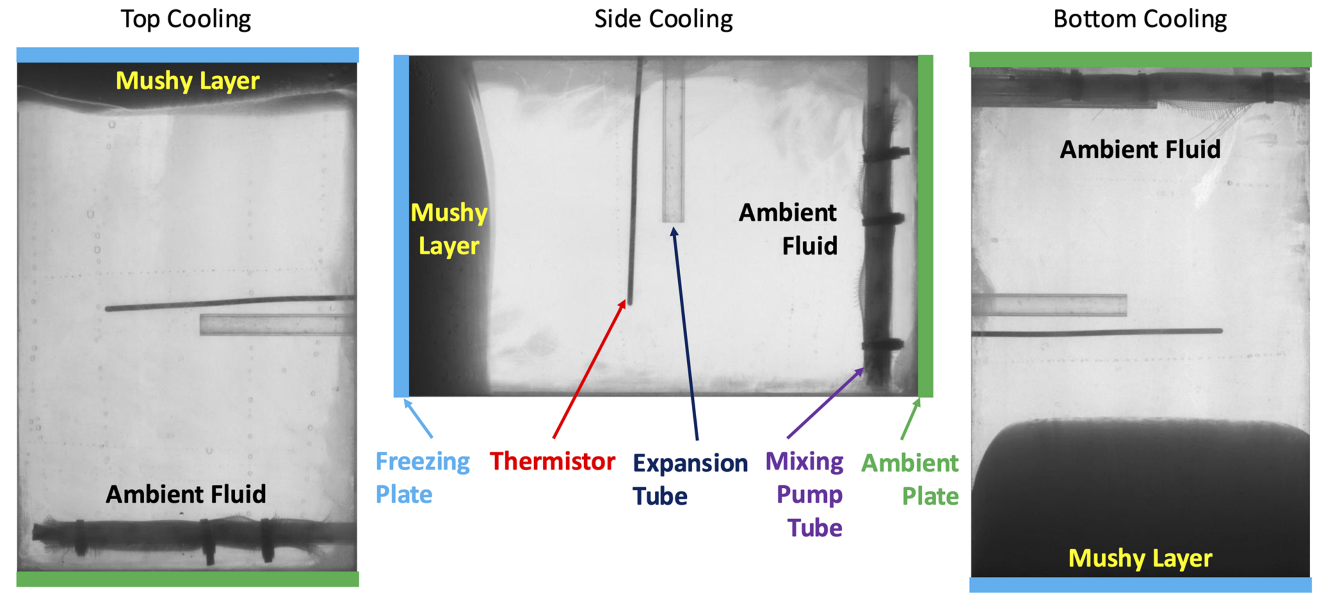

Figure 3. Photos of the equilibrated mushy layer for the top, side and bottom freezing directions (left to right) for experiments with initial ambient salinities of S_o = 33 g kg⁻1 and freezing plate temperatures of $T_{FP} = -20$°C. In each photo, the positions of the freezing and ambient plates are indicated by the blue and green boundaries, respectively; the thermistor, expansion tube and shrouded mixing pump tube are visible as indicated in the photo of the side cooling case.

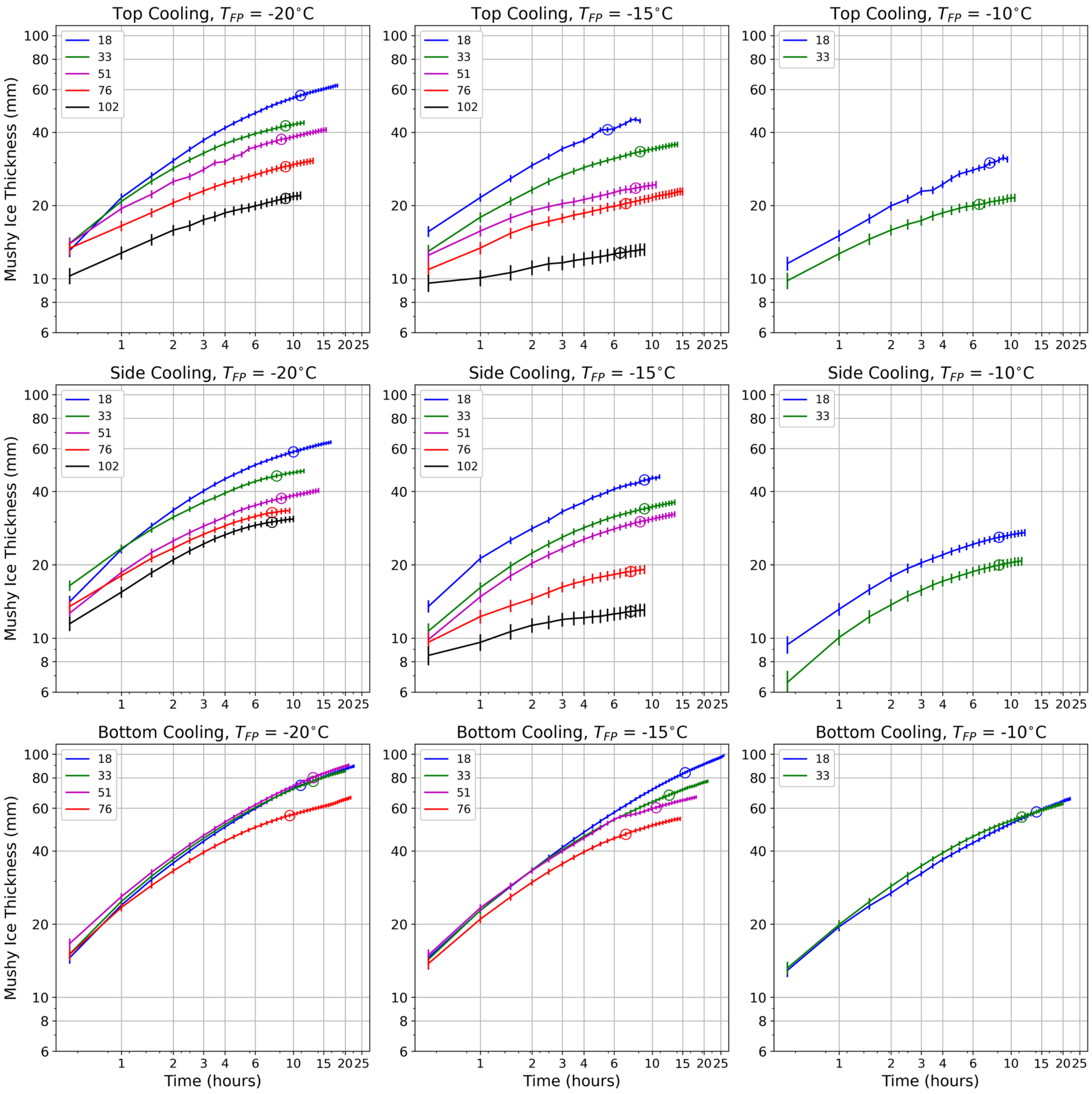

Figure 4. The time evolution of bulk mushy layer thickness for all experiments; the columns indicate the different freezing plate temperatures increasing from left to right, and the rows indicate the different freezing directions. The line colours represent the different initial ambient salinities (see legend; in g kg^{-1}). The vertical dashes indicate the times that photos were taken, and their extent is indicative of the measurement uncertainty. The circles represent the bulk mushy layer thickness when the experiment has reached equilibrium.

for the top and side cooling cases; experiments with higher initial salinities and warmer freezing plate temperatures exhibited reduced mushy layer thicknesses and growth rates. The bottom cooling experiments exhibited less sensitivity to the initial ambient salinity and freezing plate temperature, and faster growth rates.

Figure 5 shows the initial (based on the initial ambient fluid salinity S_o and the freezing plate temperature T_{FP}) and final interior ice conditions. The ice interior temperature characterises the bulk thermal conditions of the ice. The ice bulk salinity reflected the ratio of the total mass of salt contained in brine within the mushy layer (in grams) to the total mass of the mushy layer and brine mixture (in kilograms); this was the salinity of the aqueous solution that resulted from the melting of the mushy layer. Here, the initial ice bulk salinity was assumed to be that of the initial ambient fluid salinity S_o, and the initial ice interior temperature was that of the freezing plate T_{FP}. The final ice interior temperature $T^\star$ was given by Eqn (9), where we used the freezing plate temperature T_{FP}, and the liquidus temperature T_{liq} based on the final ambient salinity S_f. The final ice bulk salinity $S^\star$ was calculated using the solid fraction ϕ and the average of the brine salinities S_b obtained with Eqn (10) from the freezing plate temperature T_{FP} and the liquidus temperature T_{liq}; the relationship between the ice bulk salinity, brine salinity and solid fraction was,

$$\phi = 1 - \frac{S^\star}{S_b} \quad \Rightarrow \quad S^\star = (1 - \phi) S_b. \tag{14}$$

Here for ϕ we used the average value of ϕ_S and ϕ_M (recall ϕ_S and ϕ_M are the solid fractions calculated by the salt mass and total

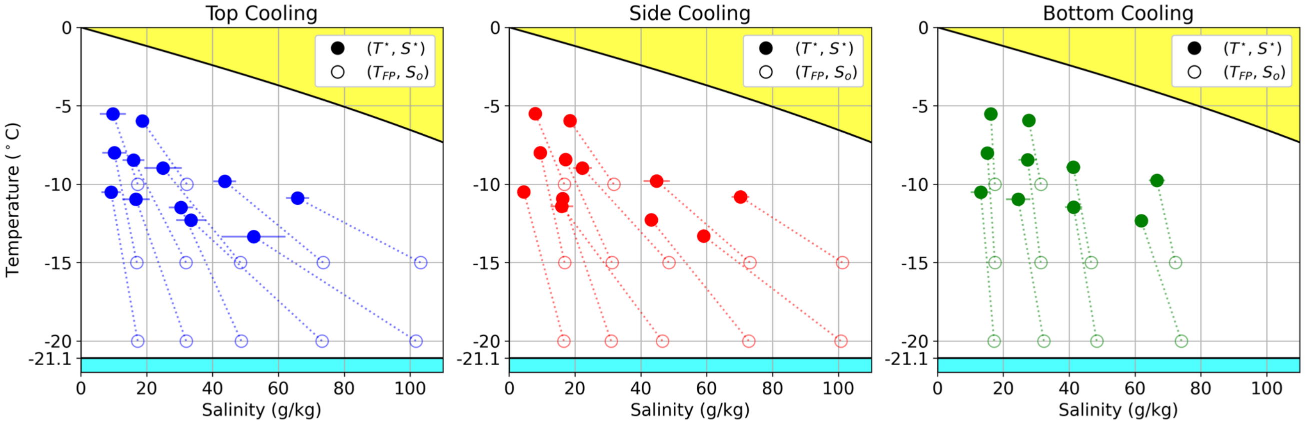

Figure 5. The initial (hollow circles) and final (solid circles) ice temperatures and salinities of the top, side and bottom (left to right) cooling experiments. We approximate the initial ice temperature and salinity conditions as the freezing plate temperature T_{FP} and the initial ambient salinity S_o, respectively. The final ice temperature and salinity conditions are the final ice interior temperature $T^\star$ (Eqn (9)) and the final ice bulk salinity $S^\star$ (Eqn (14)), respectively. As $S^\star$ is calculated with the solid fraction ϕ, we use both the total mass and salt mass conservation methods to obtain two values of $S^\star$ and take the average; the horizontal lines through the solid circles represent the range of $S^\star$ from ϕ_S and ϕ_M. The yellow, white and blue regions represent the aqueous solution, mushy layer and compositional mushy layer regimes, respectively, as per Figure 1.

mass conservation methods, respectively; Eqns (3) and (5)), and provided an indication of the differences of ice bulk salinities estimated by the two different methods (the left and right tips of the horizontal lines through the solid circles reflect the two different $S^\star$ calculated by the two different ϕ).

The final ice interior temperature was, by definition, always warmer than the initial ice interior temperature. The final ice bulk salinity was fresher than the initial ice bulk salinity for the top and side cooling cases; for the bottom cooling, however, the initial and final ice bulk salinities were virtually the same. This freshening of the ice bulk salinity reflected the gravity drainage of salty brine from the mushy layer in the top and side cooling cases, which is a process that is not able to occur in the bottom cooling experiments.

The solid fractions calculated by the total mass and salt mass conservation methods over the course of each experiment are shown in Figure 6. In general, the solid fractions decreased for increasing ambient salinities, and warming freezing plate temperatures. The experiments with top and side cooling cases exhibited solid fractions that increased in time, and the rate at which these solid fractions increased tends to increase with ambient salinity; the similarities between the solid fraction evolutions of the top and side cooling cases reflect the fact that brine diffusion does not contribute significantly to sea-ice desalination (e.g. Notz and Worster, 2009). The bottom cooling experiments tended to remain near their initial solid fractions.

The initial ice bulk salinity (approximated by the initial ambient fluid salinity S_o) and the ice interior temperature T_{ice} can be used with Eqns (10) and (14) to calculate a predicted solid fraction, which are shown in Figure 6 as horizontal lines. These predicted solid fractions exhibited good agreement with the measured ϕ during early stages, and throughout for the bottom cooling experiments. Interestingly, while the top and bottom cooling experiments tended to have larger ϕ_S relative to ϕ_M, the side cooling experiments have larger ϕ_M; the reason for this is unknown.

The effect of the freezing direction on the evolution of the mushy layer is represented in Figure 7, which shows timeseries of the bulk mushy layer thickness and solid fractions for all cases with initial ambient fluid salinity $S_o = 33\,\text{g}\,\text{kg}^{-1}$. For all three freezing plate temperatures, the bottom cooling cases have the largest rate of bulk mushy layer thickness increase. The top and side cooling cases exhibit similar bulk mushy layer thickness evolutions for all T_{FP}, and final thicknesses of approximately half that of the respective bottom cooling case. The solid fraction timeseries also highlight similarities between the solid fraction evolutions of the top and side cooling cases, while the evolutions of the bottom cases appear substantially different. Indeed, the solid fractions of the bottom cooling cases remain near to the predicted initial solid fraction values, which, understandably, are indistinguishable for the different cases because they share common initial ambient fluid salinities and freezing plate temperatures.

The equilibrated solid fractions were sensitive to the salinity and temperature conditions of the system. Figure 8 shows the measured solid fractions of the experiments plotted by their respective initial ambient salinities S_o and freezing plate temperatures T_{FP} (top row), and their final ice bulk salinities $S^\star$ and interior temperatures $T^\star$ (middle row). These plots include the solid fractions predicted by Eqns (8), (9), (10) and (14) for a range of ambient salinities and freezing plate temperatures (top row) and ice bulk salinities and interior temperatures (middle row). The differences between the measured and predicted solid fractions are shown for the different freezing directions and freezing plate temperatures (bottom row).

In general, there was good agreement between the measured and predicted solid fractions; they exhibited consistent behaviours in terms of their relative sensitivities to the salinity and temperature conditions. The agreement was improved when using the final ice bulk salinities and interior temperatures instead of the initial ambient salinities and freezing plate temperatures. The agreement between the measured and predicted solid fractions was best for experiments with smaller ice bulk salinities; this makes good physical sense as the solid fraction converges to $\phi = 1$ as system freshens. The experiments with bottom cooling exhibited the best agreement for the initial conditions; this reflects the fact that brine drainage does not occur in this configuration, such that the equilibrium ice conditions were well represented by the known initial conditions. We hypothesise that the leading sources of the disagreement between the measured and predicted was uncertainty in regards to the final ice interior temperature (which we assume to be the mid-point between the freezing plate and liquidus temperatures; Eqn (9)), final ice bulk salinity (which is also subject to the assumption that the brine salinity can be approximated by the mid-point salinity between the ambient fluid salinity and the freezing plate temperature liquidus salinity), and variations throughout the mushy layer that were not well represented by the bulk approach employed here.

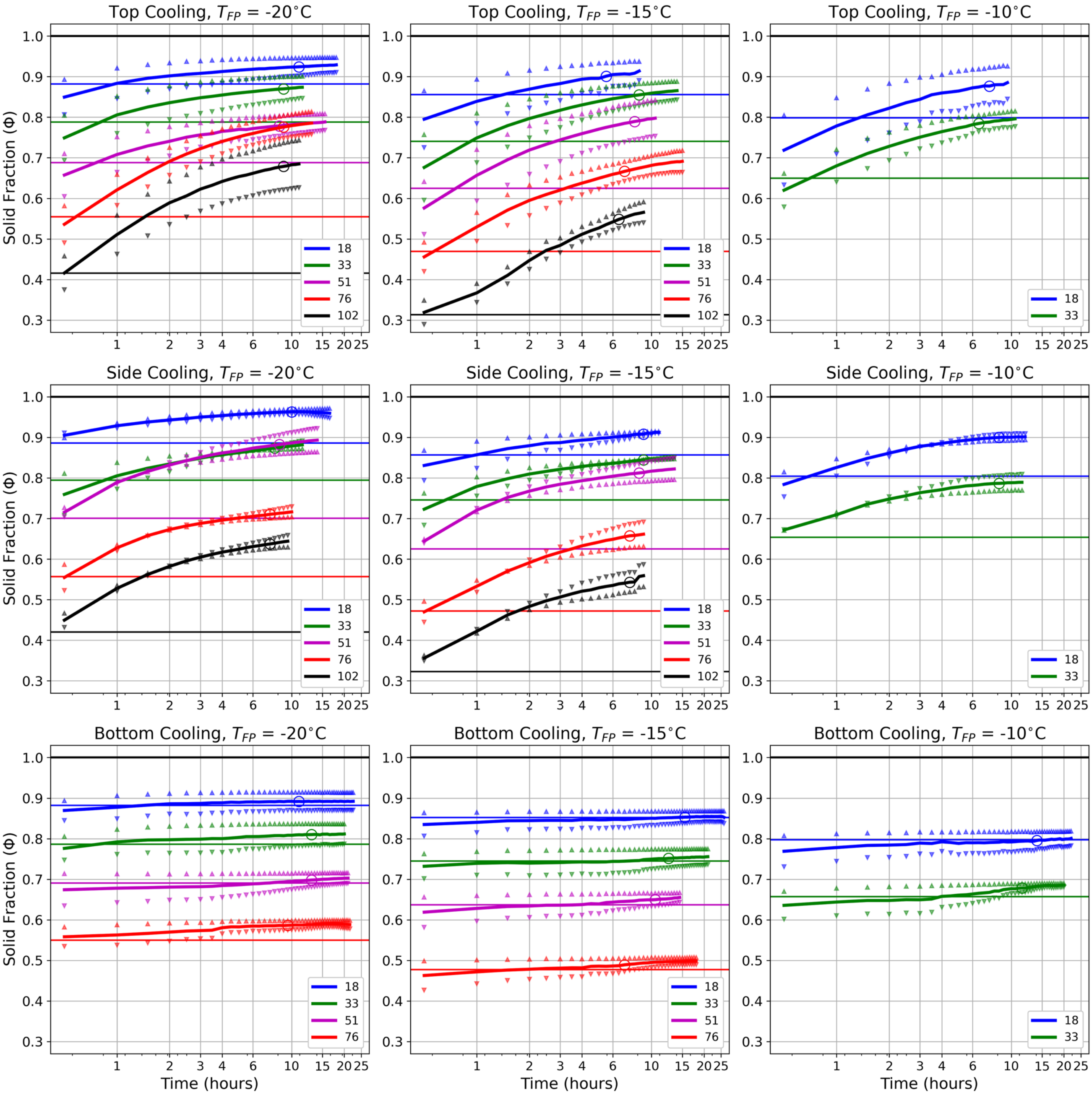

Figure 6. The time evolution of the solid fraction for all experiments; the columns indicate the different freezing plate temperatures increasing from left to right, and the rows indicate the different freezing directions. The line colours represent the different initial ambient salinities (see legend; in g kg^{-1}). The upright triangles are the solid fractions calculated with the salt mass conservation method ϕ_S; the inverted triangles are the solid fractions calculated with the total mass conservation method ϕ_M; the lines follow the average value of the two. The circles represent the solid fraction when the experiment has reached equilibrium. The horizontal lines indicate the predicted solid fraction ϕ based on the initial ice bulk salinity (approximated by S_o) and interior ice temperature T_{ice} (Eqns (10) and (14)).

The sensitivities of the measured solid fractions with respect to the final ice bulk salinities and ice interior temperatures are shown in Figure 9, plotted by the freezing plate temperature and initial ambient salinity, respectively. These were calculated by taking the mean gradient of the measured ϕ with respect to bulk ice salinity at the three different freezing plate temperatures ($\partial\phi/\partial S^{\star}|_{T_{\mathrm{FP}}}$; left panel), and the mean gradient of the measured ϕ with respect to ice interior temperature at the five different initial ambient salinities ($\partial\phi/\partial T^{\star}|_{S_o}$; right panel). Also included are the predicted sensitivities derived from the solid fraction predictions shown in Figure 8; for these we used values of $\partial\phi/\partial S^{\star}|_{T_{\mathrm{FP}}}$ at $S_o = 33\ \mathrm{g\,kg^{-1}}$ for the three freezing plate temperatures, and the mean values of $\partial\phi/\partial T^{\star}|_{S_o}$ at $T_{\mathrm{FP}} = (-20, -15, -10)$°C for the five different initial ambient salinities.

The solid fraction sensitivity to ice bulk salinity has a strong dependence on the freezing plate temperature; for a given freezing plate temperature, the rate of change of solid fraction with respect to ice bulk salinity nearly doubled from $\partial\phi/\partial S^{\star}|_{T_{\mathrm{FP}}} \approx -0.006\ (\mathrm{g/kg})^{-1}$ at $T_{FP} = -20$°C to more than $\partial\phi/\partial S^{\star}|_{T_{\mathrm{FP}}} \approx -0.01\ (\mathrm{g/kg})^{-1}$ at $T_{FP} = -10$°C. This was reflected in the convergence of the predicted solid fraction contours for warming freezing plate temperatures in Figure 8; this convergence occurs because ϕ goes from $\phi = 1$ at zero salinities to $\phi = 0$ at the liquidus salinity, which decreases for increasing temperatures. The sensitivity of the solid fraction to the ice interior temperature depended on the initial ambient salinity; the rate of change of solid fraction with ice interior temperature increased by a factor of 5 between initial ambient salinities of $S_o \approx 18$–$102\ \mathrm{g\,kg^{-1}}$.

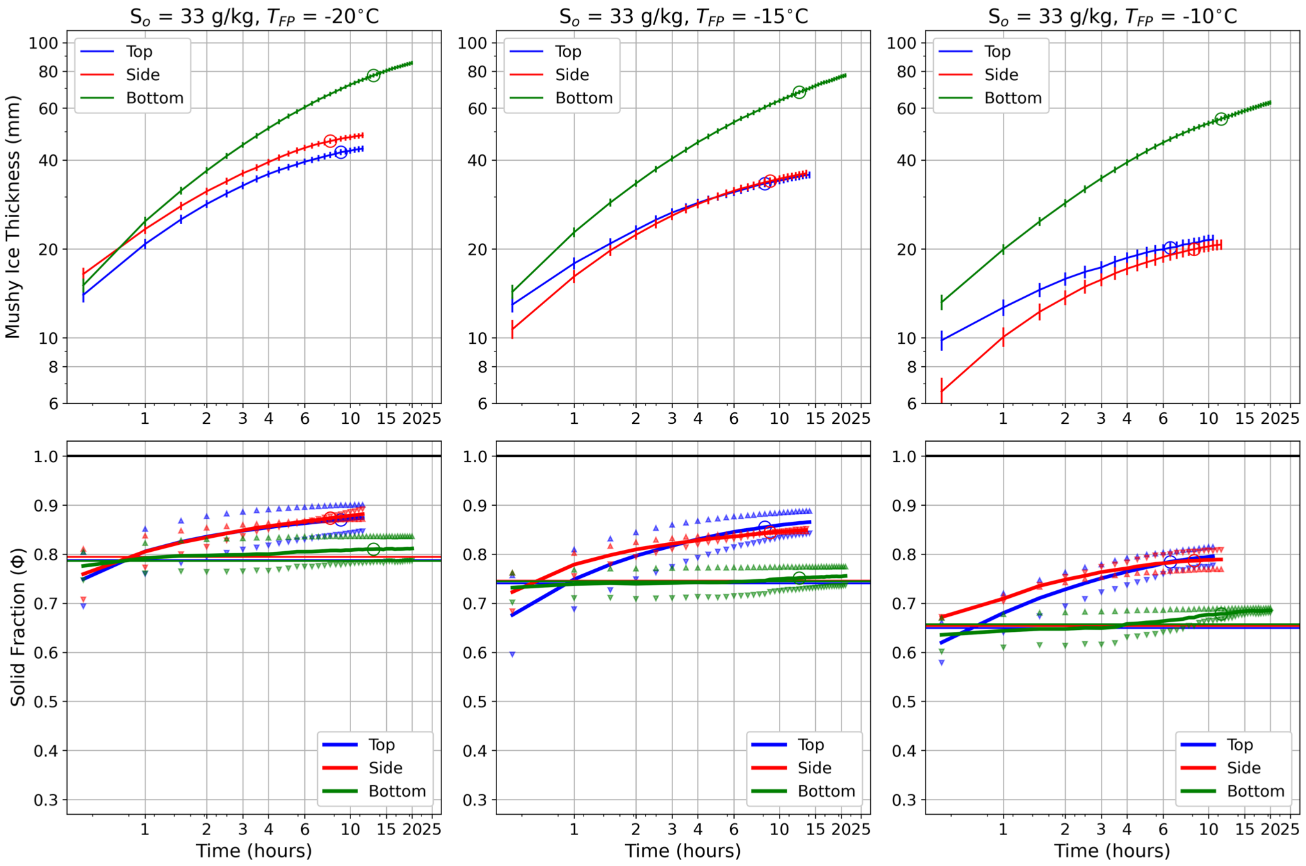

Figure 7. The time evolution of bulk mushy layer thickness (top row) and measured solid fractions (bottom row) for all experiments with $S_o = 33\,\mathrm{g\,kg^{-1}}$; these plots show a subset of the timeseries data from Figures 4 and 6, now grouped so as to highlight the differences arising from the freezing direction. The vertical dashed lines in the bulk mushy layer thickness plots are the same as those described in Figure 4; the triangles and horizontal lines in the solid fraction plots are as described in Figure 6.

There was good agreement between the measured sensitivities and those predicted by the relationship in Eqns (8), (9), (10) and (14).

The sensitivity analysis allowed us to determine whether the solid fraction was more responsive to the temperature or salinity properties of the system. For the oceanographically realistic experiments with $S_o \approx 33\,\mathrm{g\,kg^{-1}}$, the sensitivity of solid fraction to ice interior temperature was approximately $\partial\phi/\partial T^\star|_{S_o} \approx -0.02^\circ\mathrm{C}^{-1}$, or –2.5% per 1°C increase. To achieve an equivalent magnitude change in the solid fraction from a change in the ice bulk salinity requires a salinity increase of $\sim 4\,\mathrm{g\,kg^{-1}}$ at $T_{\mathrm{FP}} = -20^\circ\mathrm{C}$, or $\sim 2\,\mathrm{g\,kg^{-1}}$ at $T_{\mathrm{FP}} = -10^\circ\mathrm{C}$. When considering the relative ranges of temperature and salinity variabilities at high latitudes, this sensitivity analysis suggests that the solid fraction is temperature dominated. It follows that increases in ice interior temperature will lead to a reduction in the ice solid fraction.

5. Discussion and conclusions

The experiments demonstrate how the mushy layer growth rate and solid fraction are affected by the freezing plate temperature, ambient salinity and freezing direction. Our approach has allowed for a thorough exploration of a wide range of thermodynamic conditions and freezing directions with a single apparatus and common methodology. The results exhibited good agreement with existing theories for how the solid fraction depends on ice bulk salinity and interior temperature (e.g. Wettlaufer and others, 1997; Notz, 2005; Feltham and others, 2006). Mushy layer growth rate was largest for cooler freezing plate temperatures, fresher ambient salinities and bottom cooling cases. The equilibrated mushy layer solid fractions were largest for cooler freezing plate temperatures and fresher ambient salinities, and smallest for the bottom cooling cases where brine drainage was unable to occur. The sensitivity of the solid fraction to the ice temperature and salinity was explored, and it is found that for oceanographically realistic conditions the solid fraction was most sensitive to changes in temperature; every 1°C increase in freezing temperatures resulted in a 2.5% decrease of solid fraction.

The bottom cooling cases exhibited substantially different mushy layer behaviour and solid fraction evolution, which resulted from the absence of brine drainage. The top and side cooling cases exhibited very little difference; they had similar solid fraction evolutions, final values and sensitivities for the oceanographically relevant range of salinities (i.e. $S_o = (18,\ 33)\,\mathrm{g\,kg^{-1}}$). This finding suggests that the introduction of lateral freeze/melting in modern numerical sea-ice models (e.g. CICE6 v6.1.2), and the associated lateral sea-ice thermodynamics, should not require distinct parameterisations for solid fractions arising from vertical versus lateral sea-ice growth.

The implications of the relatively high thermal sensitivity of solid fraction are worthy of closer attention. In the experiments, the increase in freezing temperature resulted in a reduction in the solid fraction of sea ice. Before using this finding to predict sea-ice behaviour under realistic and future climate forcing scenarios (e.g. Post and others, 2019), we must first consider the extent to which the experiments are representative of the actual system. For example, the standard laboratory approach of using a freezing plate to achieve a constant temperature boundary condition (i.e. Dirichlet boundary condition) is fundamentally different to the boundary conditions experienced by actual sea ice, which are closer to a combination of a heat flux condition (i.e. Neumann

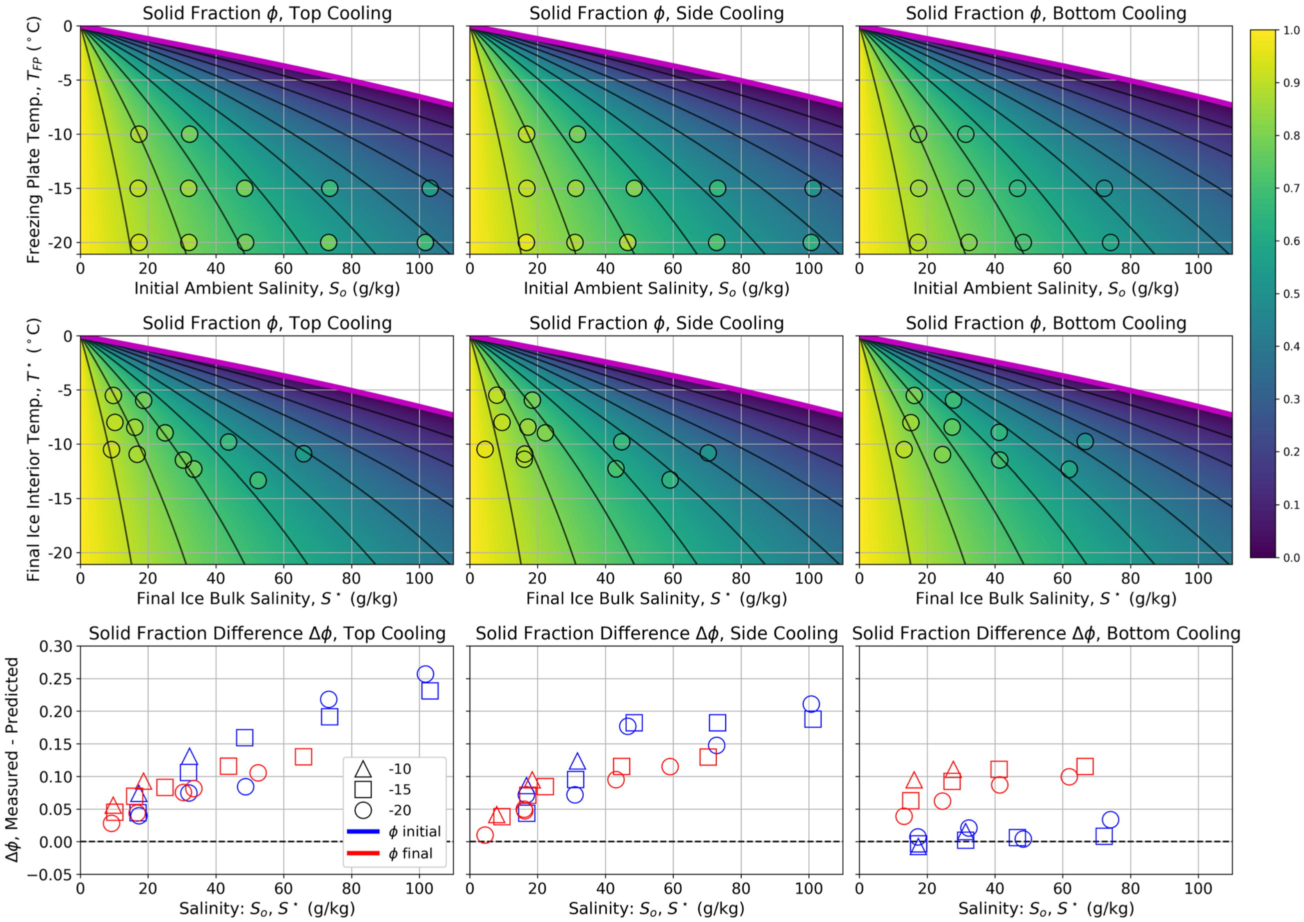

Figure 8. Measured solid fractions at equilibrium plotted by their respective freezing plate temperatures T_{FP} and initial ambient salinities S_o (top row), and their respective final ice interior temperatures $T^\star$ and bulk salinities $S^\star$ (middle row). The background colourmap indicates the solid fractions predicted by Eqns (8), (9), (10) and (14) using a range of ice bulk salinities and interior temperatures. The contours are at $\phi = 0.1$ intervals, and the magenta line represents the liquidus curve. The differences between the measured and predicted solid fractions for the initial and final ice conditions, as indicated by the differences in colour between the data points and background colourmap, are shown explicitly in the bottom row; the blue- and red-coloured datapoints indicate the initial and final solid fractions, respectively, and the datapoint shapes distinguish their freezing plate temperatures (triangle, squares, circles represent $T_{FP} = -10, \; -15, \; -20$°C, respectively).

boundary condition) and a fixed temperature condition at the phase transition point between the ocean and sea-ice boundary. That is, the real sea-ice system does not actually have a direct analogue of the laboratory freezing plate temperature, so the geophysical implications of this finding are difficult to postulate. In addition, seawater is comprised of many different salts that all

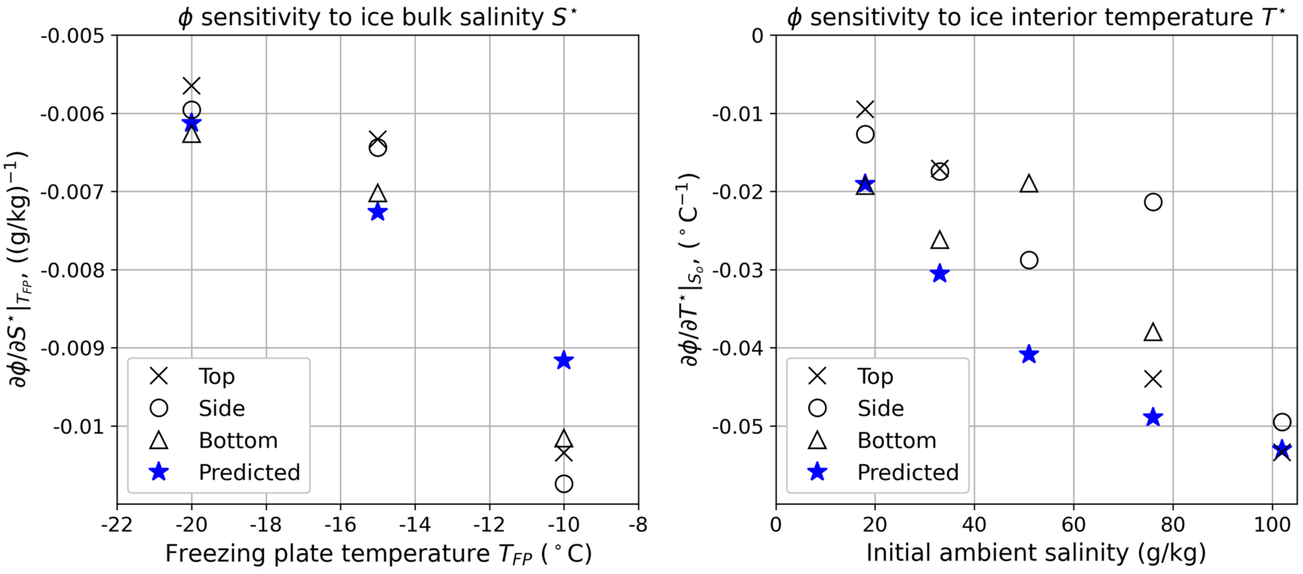

Figure 9. The sensitivities of measured solid fraction to the ice bulk salinity $\partial\phi/\partial S^\star|_{T_{FP}}$ (left) and the ice interior temperature $\partial\phi/\partial T^\star|_{S_o}$ (right) for given freezing plate temperatures and initial ambient salinities, respectively. The predicted sensitivities given by the relationships in Eqns (8), (9), (10) and (14) are also included (blue stars).

have different eutectic temperatures, which could alter the mushy layer thermodynamics from those observed here with the relatively simple aqueous solution of tapwater and NaCl; this is particularly the case for sea-ice temperatures cooler than the range explored here (i.e. cooler than $T_e = -21.1°C$). That said, future experiments could employ alternative approaches to more directly relate the laboratory sea ice and its thermodynamics to the real system.

Acknowledgements. We thank Angus Rummery and Tony Beasley for the construction of the apparatus and laboratory assistance. We also thank two reviewers for their helpful comments and suggestions that have greatly improved the scientific analysis and presentation within this manuscript.

References

Anderson D and Guba P (2020) Convective phenomena in mushy layers. *Annual Review of Fluid Mechanics* **52**, 93–119. doi: 10.1146/annurev-fluid-010719-060332

Budyko M (1969) The effect of solar radiation variations on the climate of the earth. *Tellus* **21**, 611–619.

Cox G and Weeks W (1975) Brine drainage and initial salt entrapment in sodium chloride ice. *CRREL Research Report* **345**, 88 pp. https://hdl.handle.net/11681/5820

Eayrs C and 5 others (2019) Understanding the seasonal cycle of Antarctic sea ice extent in the context of longer-term variability. *Reviews of Geophysics* **57**, 1037–1064. doi: 10.1029/2018RG000631

Feltham D, Untersteiner N, Wettlaufer J and Worster M (2006) Sea ice is a mushy layer. *Geophysical Research Letters* **33**, L14501. doi: 10.1029/2006GL026290

Foster T and Carmack E (1976) Frontal zone mixing and Antarctic bottom water formation in the southern Weddell Sea. *Deep-Sea Research* **23**, 301–317. doi: 10.1016/0011-7471(76)90872-X

Haine T and Martin T (2017) The Arctic-Subarctic sea ice system is entering a seasonal regime: implications for future Arctic amplification. *Scientific Reports* **7**, 4618. doi: 10.1038/s41598-017-04573-0

Hunke E, Lipscomb W, Turner A, Jeffery N and Elliot S (2015) CICE: the Los Alamos sea ice model documentation and software user's manual version 5.1. *Los Alamos National Laboratory.*

Huppert H (1990) The fluid mechanics of solidification. *Journal of Fluid Mechanics* **212**, 2090240. doi: 10.1017/S0022112090001938

Kraitzman N, Promislow K and Wetton B (2022) Slow migration of brine inclusions in first-year sea ice. *Society for Industrial and Applied Mathematics: Journal on Applied Mathematics* **82**, 1470–1494. doi: 10.1137/21M1440244

Manabe S and Stouffer R (1979) A CO2-climate sensitivity study with a mathematical model of the global climate. *Nature* **282**, 491–493.

Notz D (2005) *Thermodynamic and Fluid-Dynamical Processes in Sea Ice* (Ph.D. Thesis) University of Cambridge, Cambridge, UK.

Notz D and Worster M (2009) Desalination process of sea ice revisited. *Journal of Geophysical Research: Oceans* **114**, C05006. doi: 10.1029/2008JC004885

Peppin S, Aussillous P, Huppert H and Worster M (2007) Steady-state mushy layers: experiments and theory. *Journal of Fluid Mechanics* **570**, 69–77. doi: 10.1017/S0022112006003028

Pfann W (1955) Temperature gradient zone melting. *Journal of Metals* **7**, 961–964. doi: 10.1007/BF03377594

Post E and 14 others (2019) The polar regions in a 2°c warmer world. *Science Advances* **5**, 9883. doi: 10.1126/sciadv.aaw9883

Pounder E (1965) *The Physics of Ice*. Oxford, UK: Pergamon Press.

Purich A and Doddridge E (2023) Record low Antarctic sea ice coverage indicates a new sea ice state. *Nature: Communications Earth & Environment* **4**, 314. doi: 10.1038/s43247-023-00961-9

Scotti K and 6 others (2019) The effect of solidification direction with respect to gravity on ice-templated TiO2 microstructures. *Journal of the European Ceramic Society* **39**, 3180–3193. doi: 10.1016/j.jeurceramsoc.2019.04.007

Untersteiner N (1968) Natural desalination and equilibrium salinity profile of perennial sea ice. *Journal of Geophysical Research* **73**, 1251–1257. doi: 10.1029/JB073i004p01251

Vancoppenolle M, Madec G, Thomas M and McDougall T (2019) Thermodynamics of sea ice phase composition revisited. *Journal of Geophysical Research: Oceans* **124**, 615–634. doi: 10.1029/2018JC014611

Wakatsuchi M and Ono N (1983) Measurements of salinity and volume of brine excluded from growing sea ice. *Journal of Geophysical Research* **88**, 2943–2951. doi: 10.1029/JC088iC05p02943

Weast R (1971) *Handbook of Chemistry and Physics*. Cleveland, OH, USA: Chemical Rubber Company.

Weeks W (2010) *On Sea Ice*. Fairbanks, AK: University of Alaska Press.

Weeks W and Ackley S (1986) The growth, structure, and properties of sea ice. In Untersteiner N (ed.), *The Geophysics of Sea Ice*. New York, NY: Plenum Press, pp. 9–164.

Wells A, Hitchen J and Parkinson J (2019) Mushy-layer growth and convection, with application to sea ice. *Philosophical Transactions of the Royal Society A* **377**, 20180165. doi: 10.1098/rsta.2018.0165

Wettlaufer J, Worster M and Huppert H (1997) Natural convection during solidification of an alloy from above with application to the evolution of sea ice. *Journal of Fluid Mechanics* **237**, 649–669. doi: 10.1017/S0022112092003562

Worster M (1997) Convection in mushy layers. *Annual Reviews of Fluid Mechanics* **29**, 910122. doi: 10.1146/annurev.fluid.29.1.91

Worster M and Rees Jones D (2015) Sea ice thermodynamics and brine drainage. *Philosophical Transactions of the Royal Society A* **373**, 20140166. doi: 10.1098/rsta.2014.0166